

# Data-driven quasiconformal morphodynamic flows

Salem Mosleh<sup>1,2,†</sup>, Gary P. T. Choi<sup>3,†</sup>, L. Mahadevan<sup>1,4,\*</sup>

<sup>1</sup>School of Engineering and Applied Sciences, Harvard University, Cambridge, MA, USA

<sup>2</sup>Department of Natural Sciences, University of Maryland Eastern Shore, Princess Anne, MD, USA

<sup>3</sup>Department of Mathematics, The Chinese University of Hong Kong, Hong Kong

<sup>4</sup>Departments of Physics, and Organismic and Evolutionary Biology,  
Harvard University, Cambridge, MA, USA

<sup>†</sup>S.M. and G.P.T.C. contributed equally to this work.

\*To whom correspondence should be addressed; E-mail: lmahadev@g.harvard.edu

## Abstract

Temporal imaging of biological epithelial structures yields shape data at discrete time points, leading to a natural question: how can we reconstruct the most likely path of growth patterns consistent with these discrete observations? We present a physically plausible framework to solve this inverse problem by creating a framework that generalizes quasiconformal maps to quasiconformal flows. By allowing for the spatio-temporal variation of the shear and dilatation fields during the growth process, subject to regulatory mechanisms, we are led to a type of generalized Ricci flow. When guided by observational data associated with surface shape as a function of time, this leads to a constrained optimization problem. Deploying our data-driven algorithmic approach to the shape of insect wings, leaves and even sculpted faces, we show how optimal quasiconformal flows allow us to characterize the morphogenesis of a range of surfaces.

## 1 Introduction

Morphogenesis, the process by which organisms generate and regulate their shape, involves a complex interplay between biochemical and physical factors. A key goal is to identify the biophysical factors — and how they interact with biochemical signaling — that drive the local deformations and flows during morphogenesis [1]. However, often we do not obtain the local growth and flow patterns of cells from experiments, which require live imaging. Thus, working with snapshots of growing structures taken at different developmental stages, possibly from different individuals, a key mathematical challenge is to infer the local growth patterns and learn the dynamical laws that generate these structures. This requires us to determine the mapping (or flow) rules that allow us to infer the correspondence between points on the different snapshots of the growing structure. One way to address this correspondence problem is through the use of conformal maps between planar domains or even three-dimensional surfaces. These maps do not distort

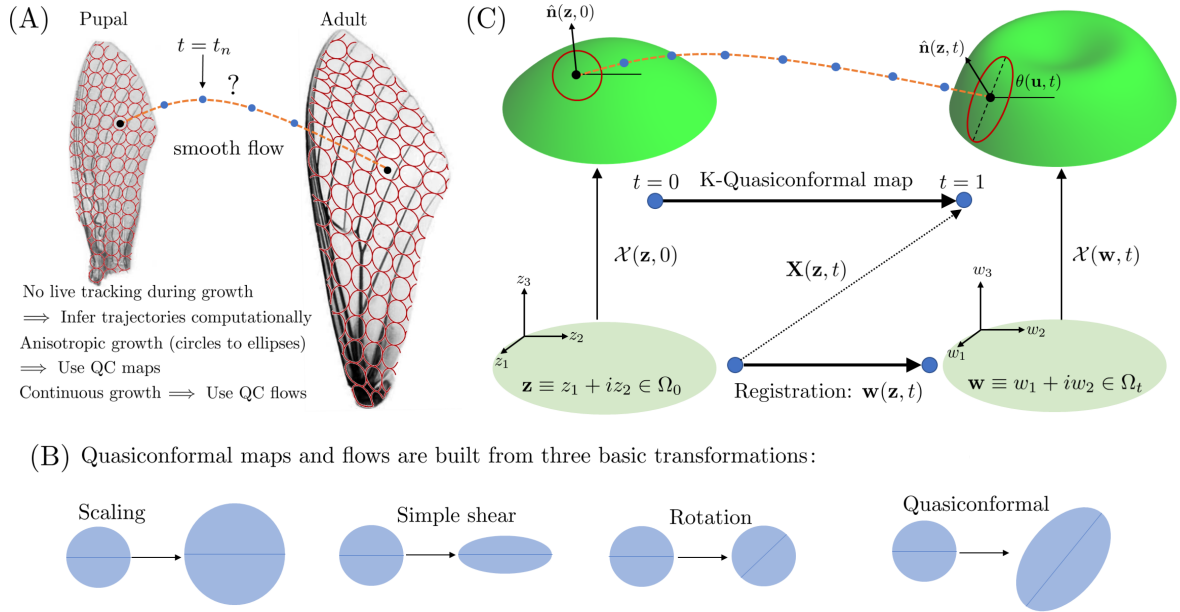


Figure 1: **Quasi-conformal flows for morphodynamics.** (A) Images of growing structures do not provide the correspondence between points at different times  $t$  (normalized by dividing with the total duration  $T$ ). We need to infer the (Lagrangian) trajectory of points computationally. (B) Quasiconformal (QC) maps and flows are useful for accomplishing this, since they describe systems that deform smoothly with anisotropic growth, where infinitesimal circles deform into infinitesimal ellipses over time due to the action of scaling, shear, and rotation fields. (C) An illustration of the geometry of deforming surfaces. Each surface, for  $t > 0$ , is given as the function  $\mathcal{X}(\mathbf{w}, t) : \Omega_t \in \mathbb{R}^2$ . Our task is to find a suitable registration  $\mathbf{w}(\mathbf{z}, t)$  that allows us to infer the true growth patterns shown in panel (A) by constricting the function  $\mathbf{X}(\mathbf{z}, t) \equiv \mathcal{X}(\mathbf{w}(\mathbf{z}, t), t)$ . Here  $\hat{\mathbf{n}}(\mathbf{z}, t)$  is the unit normal to the surface at time  $t$ .

angles [2–5]. For example given two simply connected regions in the plane, by the Riemann mapping theorem, a unique (up to Möbius transformations) conformal map exists between them and can be used to determine the correspondence between all points in the interior domains given their boundary curves. This mathematical fact has been put to use in the use of conformal maps to study growing leaves [6], insect wings [7], and other biological systems [8, 9]. Since conformal maps correspond to isotropic growth, they map infinitesimal circles to rescaled infinitesimal circles but are inadequate to describe biological growth where anisotropic growth, which distorts angles and maps infinitesimal circles to infinitesimal ellipses (Fig. 1A), is the rule rather than the exception in biological morphogenesis [10, 11]. For nearly a century, a generalization of conformal maps known as quasi-conformal maps that do account for dilatation, shear and rotation (Fig. 1B) have been known [12], although it is only recently that they have been deployed to study morphogenesis, e.g. to allow for transformations that allow for the complete set of planar deformations consistent with elastic fields, while also accounting for the presence of landmarks (points whose mapping is given *a priori* [13, 14]. When combined with different types of regularizations, e.g. minimizing squared gradients of the Beltrami fields [13]

or restrictions to smooth Teichmüller maps [14], it has been possible to study both the phylogeny and ontogeny of wing shapes using 2D quasiconformal maps. In parallel, the field of computational quasi-conformal mappings has grown rapidly with applications to complex 3D shapes such as teeth, faces etc. [15, 16].

As we gain the ability to continuously monitor growing systems, and extract their shape over time, it is natural to ask whether one can take advantage of the temporal structure of the growth process, by considering *flows* (instead of maps between discrete times points), which give smooth transformations of a shape into another shape over time [17, 18]. To this end, we generalize  $K$ -quasiconformal maps, which deform (infinitesimal) circles to ellipses whose eccentricity is bounded by the value  $K$ , to  $k$ -quasiconformal *flows* with time duration  $T$ , defined as the  $dt \rightarrow 0$  sequence of  $(kdt)$ -quasiconformal maps. Considering  $k$ -quasiconformal flows leads to interesting new mathematical problems, for example, a Teichmüller map (a  $K$ -quasiconformal map with minimal  $K$ ) between two surfaces may not be the same as the  $k$ -quasiconformal flow, with minimal  $k$ , connecting them.

As mentioned above, the prescribed data often is not sufficient (due to incomplete tracking of points) to uniquely determine a quasi-conformal map and, therefore, additional criteria are required. Common criteria involve finding the minimal distortion [19] and minimal spatial variation [13]. However, growing structures (including leaves and electrochemical interfaces) are governed by dynamical processes that couple the curvature, mechanical strain, and other fields. Here, in addition to considering minimal distortion and spatial variation flow, we find optimal quasi-conformal flows that fit the prescribed data to a dynamical equation that takes the form of a geometric partial differential equation, similar to a generalized Ricci flow. Our approach is a step towards blending data-driven and physics-based approaches since it allows us to automate the process of the discovery of growth laws and predict growth patterns from incomplete data.

This paper is organized as follows. In Section 2 we discuss the geometry and kinematics relevant to evolving surfaces and define the cost function that will be minimized in the following sections. Section 3 will discuss the discretization and numerical implementation, and Section 4 will present experiments performed on various natural and synthetic examples of flowing surfaces. We conclude our work and discuss future directions in Section 5.

## 2 Quasiconformal flows for surface registration

This section introduces the formalism for optimal quasiconformal flows and defines the cost function that we use in the following sections (see also Table 1).

### 2.1 Geometry of surface and quasiconformal maps

We start with a smooth one parameter family (flow) of surfaces  $\tilde{\mathcal{X}}(\mathbf{w}, \tilde{t})$ , which are embedded in  $\mathbb{R}^3$  with parameterization  $\mathbf{w} \in \Omega_t \subset \mathbb{R}^2$  and time  $\tilde{t} \in [0, T]$  (see Fig. 1C). We normalize lengths so that  $\mathcal{X}(\mathbf{w}, t) \equiv \tilde{\mathcal{X}}(\mathbf{w}, \tilde{t})/L$ , where  $L^2$  is the area of  $\tilde{\mathcal{X}}(\mathbf{w}, 0)$ , and normalize time so that  $t \equiv \tilde{t}/T \in [0, 1]$ . Our goal is to find a registration — a correspondence between points on the surfaces across time — as a coordinate system  $\mathbf{z} = z_1 + iz_2 \in \Omega_0 \subset \mathbb{R}^2$  and a family of maps  $\mathbf{w}(\mathbf{z}, t)$  that gives a common parameterization

Terms	Equations
Growth strain (Eq. (12))	$G_{ij}(\mathbf{z}, t) = \frac{1}{2}\dot{g}_{ij}(\mathbf{z}, t) - \lambda_1 g_{ij}(\mathbf{z}, t) - \lambda_2 H(\mathbf{z}, t)b_{ij}(\mathbf{z}, t) - \lambda_3 K(\mathbf{z}, t)g_{ij}(\mathbf{z}, t)$
Growth cost (Eq. (13))	$\mathcal{C}_{growth}[\mathbf{w}(\mathbf{z}, t)] = \int dt d\mathcal{A} \left( (A_1 - \frac{B_1}{2}) Tr [G_{ij}]^2 + B_1 Tr [G_{ij}^2] \right) + C_g \int dt \sum_{s=1}^3 \lambda_s^2(t)$
Spatial gradient cost (Eq. (18))	$\mathcal{C}_{grad}[\mathbf{w}(\mathbf{z}, t)] = A_2 \int dt d\mathcal{A} \left[ \frac{1}{2} Tr [\nabla G_{ij}]^2 + Tr [\nabla G_{ij}^2] \right]$
Bending cost (Eq. (11))	$\mathcal{C}_{bend}[\mathbf{w}(\mathbf{z}, t)] = A_3 \int dt d\mathcal{A} \dot{\mathbf{n}}^2(\mathbf{z}, t)$
Enforcing normal displacement (Eq. (15))	$\mathcal{C}_{normal}[\mathbf{w}(\mathbf{z}, t)] = C_n \int_{\mathcal{X}_i} dt d\mathcal{A} [V_{\perp}(\mathbf{z}, t) - \bar{V}_{\perp}(\mathbf{z}, t)]^2$
Enforcing boundary displacements (Eq. (16))	$\mathcal{C}_{boundary}[\mathbf{w}(\mathbf{z}, t)] = C_b \int_{\partial\mathcal{X}_i} dt ds [V_{\partial}(\mathbf{z}, t) - \bar{V}_{\partial}(\mathbf{z}, t)]^2$
Enforcing landmark velocities (Eq. (17))	$\mathcal{C}_{landmark}[\mathbf{w}(\mathbf{z}, t)] = C_L \int dt \sum_{*} [V(\mathbf{z}_{*}, t) - \bar{V}_{*}(t)]^2$
Overall cost function (Eq. (20))	$\mathcal{C}[\mathbf{w}(\mathbf{z}, t)] = \mathcal{C}_{growth} + \mathcal{C}_{grad} + \mathcal{C}_{bend} + \mathcal{C}_{normal} + \mathcal{C}_{boundary} + \mathcal{C}_{landmark}$

Models	Parameters				
	$A_1$	$B_1$	$A_2$	$A_3$	$\lambda_1, \lambda_2, \lambda_3$
Conformal	✓				
Viscous	✓	✓		✓	
Uniform			✓		
Geometric	✓	✓			✓

Table 1: **The cost and parameter choices for optimal quasiconformal flows.** The first table lists the terms and equations in the models. The growth strain is the difference between the strain rate tensor  $\dot{g}_{ij}$  and the value predicted from the geometric flow.  $\mathcal{C}_{growth}$  penalizes non-zero growth strain tensor, while  $\mathcal{C}_{grad}$  penalizes spatial variations. The bending energy  $\mathcal{C}_{bend}$  penalizes changes in the shape that do not stretch the surface and the last three costs enforce the constraints from data. The second table shows the choices of parameters that we employ in different models: Conformal ( $A_1 = 1$ , and all other parameters zero), which generates a conformal fit to the flow; Viscous ( $A_1 = B_1 = A_3 = 1$ , and all other parameters zero), which generates a minimal distortion fit to the flow; Uniform ( $A_2 = 0.1$ , all other parameters zero), which minimizes the variation of the flow in space; Geometric ( $A_1 = B_1 = 1, C_g = 0.1$ , solve for  $\lambda_1, \lambda_2, \lambda_3 \neq 0$ , and all other parameters zero), which fits the flow to a dynamical equation, which is a geometric flow in the example considered in this paper. Constraints are enforced by choosing  $C_n = C_b = C_L = 10^5$  for all models.

of the surface across time,  $\mathbf{X}(\mathbf{z}, t) \equiv \mathcal{X}(\mathbf{w}(\mathbf{z}, t), t) : \Omega_0 \rightarrow \mathbb{R}^3$ . Thus, for a fixed  $\mathbf{z}$ , the function  $\mathbf{X}(\mathbf{z}, t)$  gives the trajectory of the “same” point evolving over time (orange dashed curve in Fig. 1C) and our task is to obtain these trajectories.

For notational convenience, we will express the coordinate vector as  $\mathbf{z} \equiv z_i$  ( $i = 1, 2$ ), and define derivative operators as  $\partial_i \equiv \partial/\partial z_i$ . Furthermore, we will use the Einstein summation convention, where pairs of repeated indices in an expression are summed over. Using this notation and the chain rule, a tangent vector to the surface that connects two infinitesimally separated points  $z_i$  and  $z_i + dz_i$  at time  $t$  can be written as  $d\mathbf{X}(\mathbf{z}, t) = \partial_i \mathbf{X}(\mathbf{z}, t) dz_i$ .

To describe the kinematics of growing surfaces, it is useful to consider how angles and lengths change as the surface evolves. The length squared of the line segment connecting the points  $z_i$  and  $z_i + dz_i$  is given by

$$d\ell^2(t) = |d\mathbf{X}(\mathbf{z}, t)|^2 = g_{ij}(\mathbf{z}, t) dz_i dz_j, \quad g_{ij}(\mathbf{z}, t) \equiv \partial_i \mathbf{X}(\mathbf{z}, t) \cdot \partial_j \mathbf{X}(\mathbf{z}, t), \quad (1)$$

where  $g_{ij}(\mathbf{z}, t)$  gives the components of the metric tensor in the  $z_i$  coordinate system. Using the metric tensor, we can define lengths of (and therefore angles between) line segments on the surface at time  $t$ . The matrix inverse of the metric is denoted (with upper indices) as  $g^{ij}(\mathbf{z}, t)$ , and satisfies  $g^{ij}(\mathbf{z}, t)g_{jk}(\mathbf{z}, t) = \delta_{ik}$ , where  $\delta_{ik}$  is the Kronecker delta.

Next, we describe the metric changes in terms of rotations, dilations, and shear of the tangent plane. To facilitate this, we consider the Cartesian coordinates on the plane tangent to the surface  $\mathbf{X}(\mathbf{z}, 0)$  at  $\mathbf{z}$ , which we denote as  $\tilde{\mathbf{z}}$ . The Jacobian of the transformation between  $\tilde{\mathbf{z}}$  and  $\mathbf{z}$  is given by  $\mathbf{J}_i(\mathbf{z}) \equiv \partial_i \tilde{\mathbf{z}}(\mathbf{z})$  and the initial metric is given by  $g_{ij}(\mathbf{z}, 0) = \mathbf{J}_i^\dagger(\mathbf{z}) \cdot \mathbf{J}_j(\mathbf{z})$ , where the superscript  $\dagger$  indicates a vector or matrix transpose. As the surface evolves over time, the tangent plane at  $\mathbf{X}(\mathbf{z}, 0)$  will be convected by the flow and will undergo rotation, dilation, and shear that we explicitly account for using a polar decomposition of the deformation gradient of the tangent plane followed by a coordinate transform, using the Jacobian  $\mathbf{J}_i(\mathbf{z})$ , which leads to the following expression for the metric tensor at time  $t$ ,

$$g_{ij}(\mathbf{z}, t) = \omega(\mathbf{z}, t) \mathbf{J}_i^\dagger(\mathbf{z}) \mathbf{R}^\dagger(\mathbf{z}, t) \mathbf{E}(\mathbf{z}, t) \mathbf{R}(\mathbf{z}, t) \mathbf{J}_j(\mathbf{z}), \quad \mathbf{E}(\mathbf{z}, t) \equiv \begin{pmatrix} 1 + e(\mathbf{z}, t) & 0 \\ 0 & \frac{1}{1+e(\mathbf{z}, t)} \end{pmatrix}, \quad (2)$$

where the scalar  $\omega(\mathbf{z}, t) > 0$  is the conformal factor giving the dilation of the transformation,  $e(\mathbf{z}, t) \geq 0$  relates to the eccentricity of an ellipse at time  $t$  that started as infinitesimal circle on  $\mathbf{X}(\mathbf{z}, 0)$ , with  $1 + e(\mathbf{z}, t)$  being the ratio of major to minor axes and transformations for which  $1 + e(\mathbf{z}, t) \leq K$  would be called  $K$ -quasiconformal. The 2D rotation matrix  $\mathbf{R}(\mathbf{z}, t)$  gives the direction of the major axes of the ellipse in the tangent plane at  $\mathbf{z}$  (see Fig. 1). The Beltrami coefficient [12] of this transformation is then defined as

$$\mu(\mathbf{z}, t) = \frac{e(\mathbf{z}, t)}{2 + e(\mathbf{z}, t)} \exp[-2i\theta(\mathbf{z}, t)] \quad (3)$$

where  $\theta(\mathbf{z}, t)$  is the rotation angle defining the matrix  $\mathbf{R}(\mathbf{z}, t)$ .

In addition to length, the curvature of line segments on the surface will be a useful measure of its geometry. For a curve on the surface tangent to the line segment connecting the points  $z_i$  and  $z_i + dz_i$ , whose length is given in (1), the normal curvature is defined as the projection of the curvature of the curve in space,  $\boldsymbol{\kappa}$ , in the direction of the unit normal to the surface  $\hat{\mathbf{n}}(\mathbf{z}, t)$ . Thus, we write

$$\kappa_N \equiv \boldsymbol{\kappa} \cdot \hat{\mathbf{n}}(\mathbf{z}, t) = b_{ij}(\mathbf{z}, t) \frac{dz_i}{d\ell} \frac{dz_j}{d\ell}, \quad b_{ij}(\mathbf{z}, t) \equiv \hat{\mathbf{n}}(\mathbf{z}, t) \cdot \partial_k \partial_j \mathbf{X}(\mathbf{z}, t), \quad (4)$$

where we defined the curvature tensor  $b_{ij}(\mathbf{z}, t)$ . At a given point on the surface, the principal directions (directions of maximum and minimum normal curvatures) will be denoted as  $\hat{\boldsymbol{\kappa}}_1(\mathbf{z}, t)$  and  $\hat{\boldsymbol{\kappa}}_2(\mathbf{z}, t)$ , with corresponding principal curvatures  $\kappa_1(\mathbf{z}, t)$  and  $\kappa_2(\mathbf{z}, t)$ . From the principal curvatures we can define the mean curvature  $H(\mathbf{z}, t) \equiv [\kappa_1(\mathbf{z}, t) + \kappa_2(\mathbf{z}, t)]/2$  and Gaussian curvature  $K(\mathbf{z}, t) \equiv \kappa_1(\mathbf{z}, t)\kappa_2(\mathbf{z}, t)$ .

## 2.2 Quasiconformal flows

In this section, we consider the temporal rate of change of the quantities defined in the previous section. Since we assume that the trajectories of registered points,  $\mathbf{X}(\mathbf{z}, t)$  are smooth in time, we can define the velocity field as

$$\mathbf{V}(\mathbf{z}, t) \equiv \dot{\mathbf{X}}(\mathbf{z}, t) = \mathbf{V}_\parallel(\mathbf{z}, t) + V_\perp(\mathbf{z}, t) \hat{\mathbf{n}}(\mathbf{z}, t), \quad \mathbf{z} \in \Omega_0 \quad (5)$$

where the over dot denotes a partial derivative with respect to time, and we have split the velocity into a component that is parallel to the surface, and a component along the

surface normal  $\hat{\mathbf{n}}(\mathbf{z}, t)$ . For points along the boundary of an open surface, we define the unit tangent vector to the boundary as  $\hat{\boldsymbol{\tau}}(\mathbf{z}, t)$  and write

$$\mathbf{V}_{\parallel}(\mathbf{z}, t) = V_{\tau}(\mathbf{z}, t)\hat{\boldsymbol{\tau}}(\mathbf{z}, t) + V_{\partial}(\mathbf{z}, t)\hat{\mathbf{n}}_{\partial}(\mathbf{z}, t), \quad \hat{\mathbf{n}}_{\partial}(\mathbf{z}, t) \equiv \hat{\boldsymbol{\tau}}(\mathbf{z}, t) \times \hat{\mathbf{n}}(\mathbf{z}, t), \quad \mathbf{z} \in \partial\Omega_0. \quad (6)$$

The components of the velocity normal to the surface and normal to the boundary curve,  $V_{\perp}(\mathbf{z}, t)$  and  $V_{\partial}(\mathbf{z}, t)$ , will be independent of registration since changing the registration  $\mathbf{w}(\mathbf{z}, t)$  at time  $t$  can only move the points parallel to the surface  $\mathbf{X}(\mathbf{z}, t)$  [20]. Therefore, the task of finding the registration  $\mathbf{w}(\mathbf{z}, t)$  given a flow of surfaces  $\mathcal{X}(\mathbf{w}, t)$  is equivalent to finding  $\mathbf{V}_{\parallel}(\mathbf{z}, t)$  given the perpendicular velocities  $V_{\perp}(\mathbf{z}, t)$  and  $V_{\partial}(\mathbf{z}, t)$ .

Next, we consider the rate of change of the metric, or strain rate tensor, which can be found by taking the time derivative of Eq. (1),

$$\dot{g}_{ij}(\mathbf{z}, t) = \partial_i \mathbf{X}(\mathbf{z}, t) \cdot \partial_j \mathbf{V}(\mathbf{z}, t) + \partial_i \mathbf{V}(\mathbf{z}, t) \cdot \partial_j \mathbf{X}(\mathbf{z}, t). \quad (7)$$

Note that, for a fixed registration, the coordinate  $\mathbf{z}$  represents a Lagrangian (material) coordinate system and therefore the time derivative of the metric tensor is well-defined. The rate of change of the metric may also be expressed using the decomposition given in Eq. (2),

$$\dot{g}_{ij} = \frac{\dot{\omega}}{\omega} g_{ij} + \frac{\dot{e} \omega}{1+e} \mathbf{J}_i^{\dagger} \mathbf{R}^{\dagger} \mathbf{E} \sigma_Z \mathbf{R} \mathbf{J}_j + \omega \mathbf{J}_i^{\dagger} \left[ \dot{\mathbf{R}}^{\dagger} \mathbf{R}, \mathbf{R}^{\dagger} \mathbf{E} \mathbf{R} \right] \mathbf{J}_j, \quad \sigma_Z = \begin{pmatrix} 1 & 0 \\ 0 & -1 \end{pmatrix}, \quad (8)$$

where  $[M_1, M_2] \equiv M_1 M_2 - M_2 M_1$ . The three terms in this expression represent changes in the metric due to dilations, shears, and rotations respectively. The above expression allows us to extract the dilation and shear rates as:

$$\mathcal{D}^2(\mathbf{z}, t) \equiv \frac{1}{2} \text{Tr} [\dot{g}_{ij}(\mathbf{z}, t)]^2 \equiv \frac{1}{2} (g^{ij}(\mathbf{z}, t) \dot{g}_{ij}(\mathbf{z}, t))^2 = \left( \frac{\dot{\omega}(\mathbf{z}, t)}{\omega(\mathbf{z}, t)} \right)^2, \quad (9)$$

$$\mathcal{S}^2(\mathbf{z}, t) \equiv \frac{1}{2} \text{Tr} [\{\dot{g}_{ij}(\mathbf{z}, t)\}^2] = \left( \frac{\dot{e}(\mathbf{z}, t)}{1+e(\mathbf{z}, t)} \right)^2 + \frac{[2+e(\mathbf{z}, t)]^2 e^2(\mathbf{z}, t) \dot{\theta}^2(\mathbf{z}, t)}{[1+e(\mathbf{z}, t)]^2}, \quad (10)$$

where  $\{\dot{g}_{ij}(\mathbf{z}, t)\}$  is the traceless part of the strain rate tensor. Note that the quantities  $\mathcal{D}(\mathbf{z}, t)$  and  $\mathcal{S}(\mathbf{z}, t)$  are instantaneous quantities, depending only on the change in the metric at time  $t$ , whereas  $\omega(\mathbf{z}, t)$ ,  $e(\mathbf{z}, t)$  and  $\theta(\mathbf{z}, t)$  depend on the initial surface, with  $\omega(\mathbf{z}, 0) = 1$  and  $e(\mathbf{z}, 0) = 0$ .

The quantities described so far in this section are intrinsic (depending on the metric) and do not quantify changes in embedding. For example, when unrolling a cylinder into a flat sheet, the strain rate tensor would vanish,  $\dot{g}_{ij}(\mathbf{z}, t) = 0$ . To account for changes in embedding that do not stretch the surface (isometric deformations), we will use the rate of change of the unit normal,  $\dot{\mathbf{n}}(\mathbf{z}, t) \equiv \partial \hat{\mathbf{n}}(\mathbf{z}, t) / \partial t$ , as described in Ref. [21], to write a bending-like term in the cost function as

$$\mathcal{C}_{bend}[\mathbf{w}(\mathbf{z}, t)] = A_3 \int dt d\mathcal{A} \dot{\mathbf{n}}^2(\mathbf{z}, t), \quad (11)$$

where the area element is defined using the determinant of the metric,  $g(\mathbf{z}, t)$ , as  $d\mathcal{A} \equiv dz_1 dz_2 \sqrt{g(\mathbf{z}, t)}$  and  $A_3$  is a dimensionless constant.

## 2.3 Flow rules

In this section, we consider the criteria by which a quasiconformal flow is uniquely selected from the many possible ones that fit the given data  $\mathcal{X}(\mathbf{w}, t)$ . In addition to common choices that focus on the parsimony of the mapping — such as minimizing an energy that measures the extent of the distortion and its spatial variation — we incorporate dynamical processes that generate and regulate morphogenetic flows into our framework. For concreteness, we consider shapes that may be generated from a combination of Ricci flows [22] and mean curvature flows [23], which may be relevant for growing leaves, beaks, and bacterial cell shapes [24–27]. To accomplish this, we define a growth strain tensor which is the difference between the strain rate tensor  $\dot{g}_{ij}$  and the predicted value based on the dynamical law, which can be written as an expansion involving terms proportional to the metric and curvature tensors [28],

$$G_{ij}(\mathbf{z}, t) = \frac{1}{2}\dot{g}_{ij}(\mathbf{z}, t) - \lambda_1 g_{ij}(\mathbf{z}, t) - \lambda_2 H(\mathbf{z}, t)b_{ij}(\mathbf{z}, t) - \lambda_3 K(\mathbf{z}, t)g_{ij}(\mathbf{z}, t), \quad (12)$$

where the dimensionless parameters  $\lambda_\star$  are independent of  $\mathbf{z}$  but may depend on time. If the flow  $\mathcal{X}(\mathbf{w}, z)$  is in fact generated by the dynamical law, there exists a registration  $\mathbf{w}(\mathbf{z}, t)$  such that  $G_{ij}(\mathbf{z}, t) = 0$ . For such flows, the  $\lambda_1$  term gives exponential rate of expansion or contraction, the  $\lambda_2$  term is related to the mean curvature flow, while the  $\lambda_3$  term is related to the Ricci flow [28].

To find a quasiconformal flow that is as close to satisfying  $G_{ij}(\mathbf{z}, t) = 0$  as possible, we will add the following terms to the cost function

$$\mathcal{C}_{growth}[\mathbf{w}(\mathbf{z}, t)] = \int dt d\mathcal{A} \mathcal{K}_1^{ijkl} G_{ij} G_{kl}(\mathbf{z}, t) + C_g \int dt [\lambda_1^2(t) + \lambda_2^2(t) + \lambda_3^2(t)], \quad (13)$$

where  $C_g$  is a dimensionless regularising constant and  $\mathcal{K}_1^{ijkl}$  is an isotropic rigidity matrix, which we parameterize as,

$$\mathcal{K}_1^{ijkl}(\mathbf{z}, t) \equiv (A_1 - B_1/2)g^{ij}(\mathbf{z}, t)g^{kl}(\mathbf{z}, t) + B_1 g^{ik}(\mathbf{z}, t)g^{jl}(\mathbf{z}, t), \quad (14)$$

where  $A_1$  (analogous to bulk modulus) and  $B_1$  (shear modulus) are dimensionless constants. Note that when setting  $\lambda_1 = \lambda_2 = \lambda_3 = 0$ , Eq. (13) measures the extent of the distortion, since  $G_{ij}(\mathbf{z}, t)$  reduces to  $\dot{g}_{ij}(\mathbf{z}, t)/2$  in that case.

## 2.4 Imposing constraints and regulators

Since our goal is to find an optimal quasiconformal flow that coincides with the given data  $\mathcal{X}(\mathbf{w}, t)$ , we need to impose constraints that fix the computed flow to the data. As mentioned after Eq. (6), this amounts to fixing the components of the velocity field that are normal to the surface and its boundary curve, while allowing the tangent components of the velocity field to vary. We constrain the normal components by adding the following terms to the cost function being minimized:

$$\mathcal{C}_{normal}[\mathbf{w}(\mathbf{z}, t)] = C_n \int_{\mathcal{X}} dt d\mathcal{A} [V_{\perp}(\mathbf{z}, t) - \bar{V}_{\perp}(\mathbf{z}, t)]^2, \quad (15)$$

$$\mathcal{C}_{boundary}[\mathbf{w}(\mathbf{z}, t)] = C_b \int_{\partial\mathcal{X}} dt ds [V_{\partial}(\mathbf{z}, t) - \bar{V}_{\partial}(\mathbf{z}, t)]^2, \quad (16)$$

where  $\bar{V}_\perp(\mathbf{z}, t)$  and  $\bar{V}_g(\mathbf{z}, t)$  are the registration independent normal displacements that are prescribed by the given data, and  $C_n, C_b$  are dimensionless constants. Note that the first integral is over the area of the surface, while the second is over its boundary curve. Landmarks are points for which we know the trajectory *a priori*, either from experiments or other considerations [29]. If we take  $\mathbf{z}_*$  as the coordinate of a given landmark point, whose velocity is given by  $\bar{\mathbf{V}}_*(t)$ , we account for landmark constraints by adding the following to the cost function:

$$\mathcal{C}_{\text{landmark}}[\mathbf{w}(\mathbf{z}, t)] = C_L \int dt \sum_{\star} [\mathbf{V}(\mathbf{z}_*, t) - \bar{\mathbf{V}}_*(t)]^2, \quad (17)$$

where  $C_L$  is a dimensionless constant and we sum over all landmarks.

In addition, to avoid quasiconformal flows that rapidly vary in space, we will add the following term to the cost

$$\mathcal{C}_{\text{grad}}[\mathbf{w}(\mathbf{z}, t)] = A_2 \int dt d\mathcal{A} \mathcal{K}_2^{ijkl}(\mathbf{z}, t) \nabla_m G_{ij}(\mathbf{z}, t) \nabla^m G_{kl}(\mathbf{z}, t) \quad (18)$$

where  $\nabla_m$  is the covariant derivative [30],  $A_2$  is a constant, and  $\mathcal{K}_2^{ijkl}$  is an isotropic rigidity matrix defined as,

$$\mathcal{K}_2^{ijkl}(\mathbf{z}, t) \equiv \frac{1}{2} g^{ij}(\mathbf{z}, t) g^{kl}(\mathbf{z}, t) + g^{ik}(\mathbf{z}, t) g^{jl}(\mathbf{z}, t). \quad (19)$$

We are now in a position to define the cost function that will be used for the rest of the paper to be:

$$\mathcal{C}[\mathbf{w}(\mathbf{z}, t)] = \mathcal{C}_{\text{growth}} + \mathcal{C}_{\text{grad}} + \mathcal{C}_{\text{bend}} + \mathcal{C}_{\text{normal}} + \mathcal{C}_{\text{boundary}} + \mathcal{C}_{\text{landmark}}, \quad (20)$$

where the individual terms are defined in Eqs. (11 - 18) and the dimensionless parameters we choose are  $A_1, B_1, A_2, A_3$ , and the constraints will be enforced by choosing  $C_n = C_b = C_L = 10^5$  for all models (see Table 1). We will consider four different choices of parameters in this paper: (1) Conformal ( $A_1 = 1$ , all other parameters zero), which generates a conformal fit to the flow; (2) Viscous ( $A_1 = B_1 = A_3 = 1$ , and all other parameters zero), which generates a minimal distortion fit to the flow; (3) Uniform ( $A_2 = 0.1$ , and all other parameters zero), which minimizes the variation of the flow in space; (4) Geometric ( $A_1 = B_1 = 1, C_g = 0.1$ , solve for  $\lambda_1, \lambda_2, \lambda_3 \neq 0$ , and all other parameters zero), which fits the flow to a dynamical equation, which in this paper is a geometric flow parameterized by  $\lambda_1, \lambda_2$ , and  $\lambda_3$  (which are solved for during our fitting procedure).

## 3 Discretizing and minimizing the cost function

### 3.1 Data preparation and mesh preprocessing

To study the growth of 2D insect wings, we considered the *Manduca sexta* (tobacco hawk moth) and *Junonia coenia* (buckeye butterfly) wing data from [31]. For each species, 2D triangular meshes were constructed based on the wing images at the larval, prepupal, pupal, and adult stages using the `distmesh` package [32]. An initial registration between

each pair of consecutive stages was then computed using a variation of the mapping method in [14], where the boundary correspondence was obtained using the curvature-guided matching method in [14] and the interior correspondence was obtained using the smooth quasiconformal mapping formulation in [9]. After getting the initial registration between the four stages above, we then applied the Piecewise Cubic Hermite Interpolating Polynomial (`pchip`) function in MATLAB to get a set of wing shapes with continuous growth over 30 time steps, which then served as the starting point for our subsequent analysis. The boundary tangent and normal vectors were calculated using the MATLAB `LineNormals2D` package [33].

To study the growth of 3D plant leaves using the proposed method, we considered the *persea americana* (avocado) leaf dataset [34]. Each leaf scan consists of about 100 tracked points in  $\mathbb{R}^3$ . To create a triangular mesh for each scan, we first used the principal component analysis (`pca`) function in MATLAB to project the points onto the 2D plane and constructed a 2D Delaunay triangulation using the MATLAB `delaunay` function, with sharp triangles at the boundary removed. The planar triangulation then induced a triangulation on the set of 3D points, resulting in a triangulated leaf mesh. Next, we further applied the Taubin smoothing [35] and the Loop subdivision [36] to obtain a smooth, refined mesh with about 400 vertices. Based on the vertices and triangulation of the mesh, we then computed the principal curvatures, mean curvature and Gaussian curvature of the mesh using the MATLAB `patchcurvature` package [37]. The tangent and normal vectors of the boundaries of open surfaces were calculated using the MATLAB `frenet_robust` package [38].

### 3.2 Discretizing the cost functional

To minimize the cost function given in Eq. (20), we split the flow into a sequence of equally spaced discrete times ( $t_n = 0, 1, \dots, T$ , where  $T = 30$ ) and represent the surfaces at each time by a triangulation (see Fig. 2). For a given triangle at time  $t$ , labeled with index  $f$  and spanned by the three vertices with positions  $\mathbf{P}_0(f, t_n)$ ,  $\mathbf{P}_1(f, t_n)$ , and  $\mathbf{P}_2(f, t_n)$ , the triangle centroid will approximate the smooth surface at the point  $\mathbf{z} = \mathbf{z}_F$ :

$$\mathbf{X}(\mathbf{z}_F, t) \approx \frac{\mathbf{P}_0(f, t_n) + \mathbf{P}_1(f, t_n) + \mathbf{P}_2(f, t_n)}{3}. \quad (21)$$

The tangent plane will be spanned by the two vectors  $\mathbf{E}_1(f, t_n) \equiv \mathbf{P}_1(f, t_n) - \mathbf{P}_0(f, t_n)$  and  $\mathbf{E}_2(f, t_n) \equiv \mathbf{P}_2(f, t_n) - \mathbf{P}_0(f, t_n)$ , which point along the edges of the triangle and give the discrete analog of  $\partial_i \mathbf{X}(\mathbf{z}_F) \approx \mathbf{E}_i(f, t_n)$ . The velocity of a point is  $\mathbf{V}_i(f, t_n) \equiv [\mathbf{P}_i(f, t + \delta t) - \mathbf{P}_i(f, t)]/\delta t$ , where  $\delta t$  is the length of the time step. To approximate the velocity gradient, we write

$$\partial_i \mathbf{V}(\mathbf{z}_F, t) \approx \delta_i \mathbf{V}(f, t_n) \equiv \frac{\mathbf{E}_i(f, t + dt) - \mathbf{E}_i(f, t_n)}{dt}, \quad i = 1, 2. \quad (22)$$

The dual basis to  $\mathbf{E}_i(f, t_n)$ , denoted as  $\mathbf{E}^i(f, t_n) \approx \partial^i \mathbf{X}(\mathbf{z}_F, t)$ , are (row) vectors in  $\mathbb{R}^3$  satisfying

$$\mathbf{E}^i(f, t_n) \cdot \mathbf{E}_j(f, t_n) = \delta_j^i, \quad \mathbf{E}_i(f, t_n) \otimes \mathbf{E}^i(f, t_n) = \mathbf{Q}_{\parallel}(f, t_n), \quad (23)$$

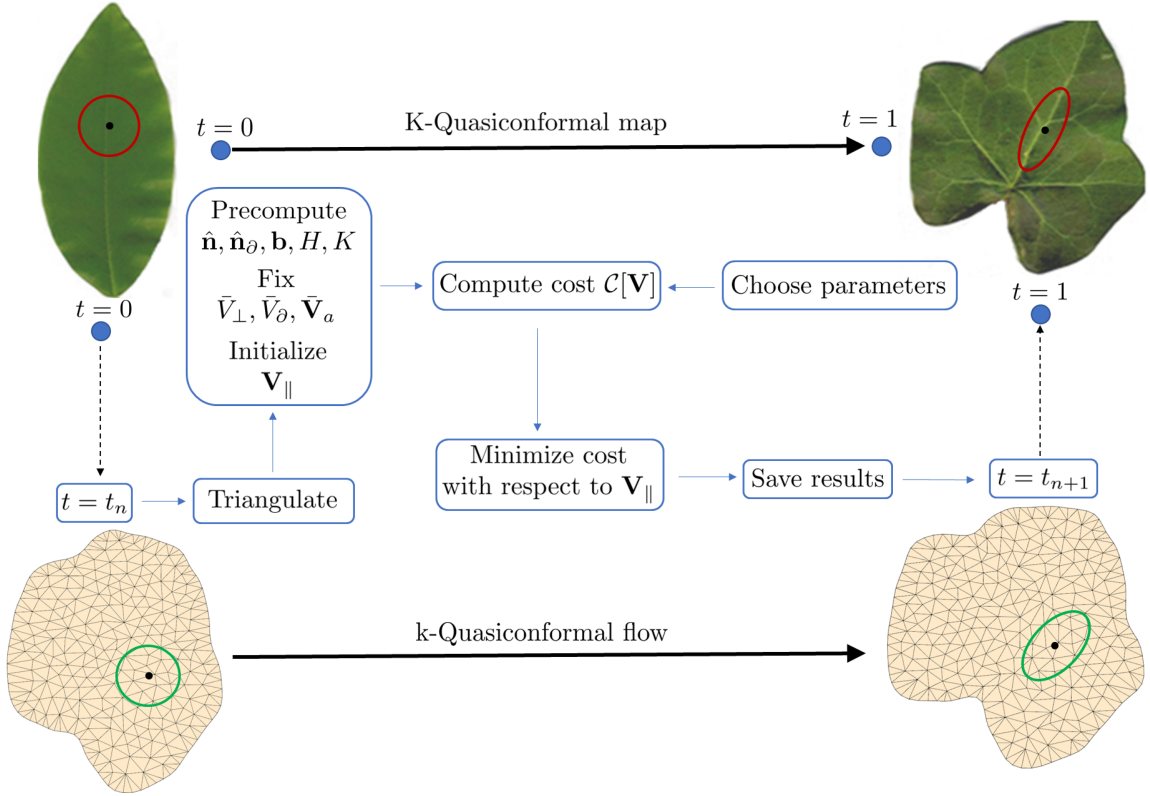


Figure 2: **Surface registration with optimal quasiconformal flows.** A  $K$ -quasiconformal map is a map between the initial ( $t = 0$ ) and final ( $t = T$ ) surfaces, where the eccentricity of ellipses on the final surface (shown in red), which are images of infinitesimal circles on the initial surface (red), are bounded by the value  $K$ . On the other hand, a  $k$ -quasiconformal flow can be thought of as a sequence of quasiconformal maps, between  $t$  and  $t + dt$ , where the eccentricity of ellipses (green) is bounded by  $kdt$ . This figure also illustrates the basic workflow in our approach: We first choose a model type from those shown in Table 1, which gives us a fixed choice of parameters in the cost function. The flow is then broken up into discrete time steps, triangulating each surface and precomputing geometric quantities that do not vary during the optimization. The optimal velocity field is calculated at time  $t = t_n$  and the results are saved before moving to the next time step.

where  $\otimes$  gives a direct product between the two vectors in  $\mathbb{R}^3$  and  $\mathbf{Q}_{\parallel}(f, t_n)$  is a  $3 \times 3$  projection matrix onto the plane of the triangle and represents an approximation of the metric tensor in the orthonormal frame spanning the plane of the triangle:

$$[\partial^i \mathbf{X} \otimes \partial^j \mathbf{X}] g_{ij}(\mathbf{z}_F, t) \approx \mathbf{Q}_{\parallel}(f, t_n). \quad (24)$$

Using Eqs. (22–23) and Eq. (7), we can approximate the strain rate tensor as

$$\begin{aligned} [\partial^i \mathbf{X} \otimes \partial^j \mathbf{X}] \dot{g}_{ij}(\mathbf{z}_F, t) &\approx \dot{\mathbf{Q}}_{\parallel}(f, t_n) \\ &\equiv \sum_{i=1}^2 [\delta \mathbf{V}_i(f, t_n) \otimes \mathbf{E}^i(f, t_n) + \mathbf{E}^i(f, t_n) \otimes \delta \mathbf{V}_i(f, t_n)]. \end{aligned} \quad (25)$$

To calculate the growth strain tensor, given in Eq. (12), we approximate the curvature tensor by

$$[\partial^i \mathbf{X} \otimes \partial^j \mathbf{X}] b_{ij}(\mathbf{z}_F, t) \approx \mathbf{B}(t) \equiv \kappa_1 \hat{\boldsymbol{\kappa}}_1 \otimes \hat{\boldsymbol{\kappa}}_1 + \kappa_2 \hat{\boldsymbol{\kappa}}_2 \otimes \hat{\boldsymbol{\kappa}}_2, \quad (26)$$

where  $\hat{\boldsymbol{\kappa}}_1(f, t_n), \boldsymbol{\kappa}_2(f, t_n)$  are unit vectors (in  $\mathbb{R}^3$ ) pointing along the principal directions for each triangle, which are calculated as described in Section 33.1, along with the corresponding principal curvatures  $\kappa_1(f, t_n), \kappa_2(f, t_n)$ . We also approximate the mean and Gaussian curvatures as  $2H(f, t_n) = \kappa_1(f, t_n) + \kappa_2(f, t_n)$  and  $K(f, t_n) = \kappa_1(f, t_n)\kappa_2(f, t_n)$ . Now, we can approximate the growth strain tensor as

$$\mathbf{G}(f, t_n) \equiv \dot{\mathbf{Q}}_{\parallel}(f, t_n) - \lambda_1 \mathbf{Q}_{\parallel}(f, t_n) - \lambda_2 H(f, t_n) \mathbf{B}(f, t_n) - \lambda_3 K(f, t_n) \mathbf{Q}_{\parallel}(f, t_n) \quad (27)$$

and compute the contribution of the triangle, at time  $t_n$ , to the distortion cost defined in Eq. (20) as

$$\mathcal{C}_{growth}[f, t_n] = \delta t \delta \mathcal{A}_F \left( (A_1 - B_1/2) \text{Tr} [G(f, t_n)]^2 + B_1 \text{Tr} [G(f, t_n)^2] \right), \quad (28)$$

where  $\delta \mathcal{A}_F$  is the area of the triangle and the total cost is found by summing over all triangles at each time step.

Having calculated the  $(3 \times 3)$  growth strain matrices  $\mathbf{G}(f, t_n)$  in Eq. (27), we proceed to estimate the discrete directional derivative, denoted as  $\mathbf{DG}_{(f\alpha)}$ , where  $f$  is the index of the corresponding face (triangle) and  $\alpha \in (1, 2, 3)$  indicates the direction of the derivative in  $\mathbb{R}^3$  (see Ref. [39] for a related approach to approximating the covariant derivative using the embedding Euclidean space). For ease of presentation, we suppressed the dependence on  $t_n$ . For a given pair of triangles connected by edge  $e$ , we denote the vector pointing from the centroid of triangle  $f$  towards its neighbor by  $\mathbf{U}_{e(f\alpha)}$ , where here again  $\alpha$  indicates the components of the vector in  $\mathbb{R}^3$ . Note that  $\mathbf{U}_{e(f\alpha)} = 0$  when  $f$  is a triangle not contained in the pair connected by edge  $e$ . We also define the finite difference matrix,  $\Delta_{ef}$ , which equals  $\Delta_{ef_1} = 1$  for the first triangle in the pair connected by edge  $e$ ,  $\Delta_{ef_2} = -1$  for the other triangle in the pair, and zero otherwise. Therefore, using a finite difference approximation, we have the relation

$$\sum_{(f\alpha)} \mathbf{U}_{e(f\alpha)} \mathbf{DG}_{(f\alpha)} = \sum_{f'} \Delta_{ef'} \mathbf{G}_{f'}. \quad (29)$$

Taking  $\mathbf{U}_{e(f\alpha)}$  as a matrix whose rows are labeled by the edge  $e$  and columns are labeled by the multi-index  $(f\alpha)$ , the above linear equation can be solved to give the covariant derivative of the growth strain tensor as

$$\mathbf{DG}_{(f\alpha)} = \sum_{f', e} \mathbf{U}_{(f\alpha)e}^+ \Delta_{ef'} \mathbf{G}_{f'}, \quad (30)$$

where  $\mathbf{U}_{(f\alpha)e}^+$  is the pseudoinverse of the matrix  $\mathbf{U}_{e(f\alpha)}$ . In order to approximate the gradient squared term in the cost function, we first define the matrix

$$\mathcal{M}_{f_1 f_2} \equiv \sum_{e_1, e_2, (f\mu)} \Delta_{e_1 f_1} \mathbf{U}_{(f\mu)e_1}^+ \mathbf{U}_{(f\mu)e_2}^+ \Delta_{e_2 f_2}, \quad (31)$$

which is positive definite since Eq. (31) has the form of a matrix times its transpose, and therefore we may formally write its square root as  $\mathcal{M}_{ff'}^{1/2}$ . The discrete growth strain gradient can then be defined as

$$\mathbf{G}_f^\nabla(t) = \sum_{f'} \mathcal{M}_{ff'}^{1/2} \mathbf{G}_{f'}, \quad (32)$$

and allows us to calculate the gradient cost for each face as in Eq. (28):

$$C_2[P_0(t), P_1(t), P_2(t)] = A_2 \delta t \delta \mathcal{A}_F \left( \frac{1}{2} \text{Tr} [\mathbf{G}_f^\nabla(t)]^2 + \text{Tr} [\mathbf{G}_f^\nabla(t)^2] \right). \quad (33)$$

## 4 Results

### 4.1 Planar shapes

Planar shapes are a special example of surfaces with boundary that are confined to the plane. In this case, all normal displacements vanish,  $\bar{V}_\perp(\mathbf{z}, t) = 0$ , and the first term of Eq. (15) is minimized by setting  $V_\perp(\mathbf{z}, t) = 0$  everywhere. We start by studying the deformation of a disc undergoing simple shear, shrinking by a factor of 1.5 in the vertical direction and expanding by the same factor in the horizontal direction over the course of 30 discrete time steps (Fig. 3).

We will perform three different minimizations, corresponding to conformal, viscous, and uniform models that are described in Table 1. The conformal model minimizes the shear rate (absolute difference in eigenvalues of the strain rate tensor) and will therefore find a nearly conformal fit to the flow (see Fig. 3). The viscous model minimizes a combination of shear dilation rates (sum of eigenvalues of the strain rate tensor), while the uniform model favors a strain rate tensor that is uniform in space. Line segments in the third row of Fig. 3 point in the same direction and have the same length, indicating a constant shear rate, while the dilation rate is zero everywhere. Note that the uniform fit to the flow recovers the constant simple shear transformation that was used to generate this test example, while the conformal and viscous fits predict a completely different growth pattern. Interestingly, as shown in the second row of Fig. 3, the viscous fits produce domains with distinct orientations and where the dilation rate changes from position (expansion) to negative (contraction).

### 4.2 Planar shapes with landmarks

In this section, we assume that a subset of the vertices of the mesh are given as landmarks, points where a trajectory  $\mathbf{x}_p(t)$  is given *a priori*, (e.g., by florescent labeling). These trajectories are enforced in the minimization procedure by adding the corresponding cost as described in Eq. (17). We perform the same three minimizations as in the previous section (see Table 1 and Fig. 3).

Figure 4 shows the results of our analysis performed on *Manduca sexta* (tobacco hawk moth) data, which was taken from [31]. For the conformal model, we observe that the more landmarks we have, the less conformal — as determined by higher values of  $\mathcal{S}/\mathcal{D}$  shown in Fig. 4 compared with SI Fig. S1. In addition, the inferred growth patterns

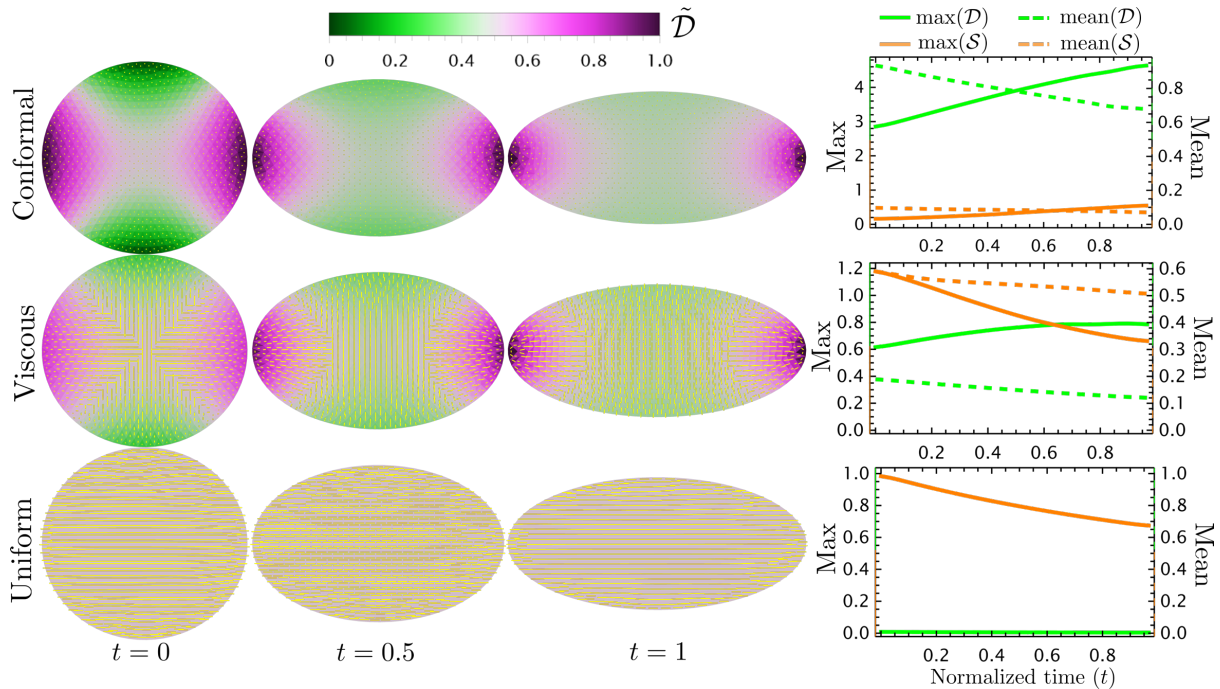


Figure 3: **Optimal 2D quasiconformal flows for a disc undergoing simple shear.** The starting point is a disc undergoing expansion by a factor of  $3/2$  in the horizontal direction, while shrinking by the same factor in the vertical, with area conserved at all times. To infer the possible growth patterns, we run the optimization with three different parameter choices given in Table 1: Conformal, Viscous, and Uniform. Here  $\mathcal{D}$  is the dilation rate given in Eq. (9) and  $\mathcal{S}$  is the shear rate given in Eq. (10). The triangles are color-coded according to the normalized dilation rate,  $\tilde{\mathcal{D}} \equiv \mathcal{D}/\max(\mathcal{D}, \mathcal{S})$ , while the length of the yellow line segments represents the magnitude of normalized shear rate,  $\tilde{\mathcal{S}} \equiv \mathcal{S}/\max(\mathcal{D}, \mathcal{S})$ , and their direction is along the largest eigen direction of the strain rate tensor. The last column shows the maximum and mean dilation and shear rates plotted against normalized time for the different registrations in each row.

depend on the assumed model, just as in the disc example (Fig. 3). For example, in the absence of landmark constraints (SI Fig. S1), the conformal model contains area shrinking (green regions) and expansion (purple regions), while the elastic and uniform models contain only area expansion. Interestingly, we observe that the proximal and distal parts of the wing behave differently in all models with a wave of expansion moving from the proximal to the distal direction over time (see SI Movie S1).

The corresponding results for *Junonia coenia* (buckeye butterfly) wing data, also taken from [31], are shown in Fig. 5 (see also SI Figs. S2). In this case, the transformation appears to be more conformal (isotropic) in nature, with the viscous and uniform models exhibiting higher dilation rates compared with shear rates.

### 4.3 Closed surfaces

For surfaces embedded in 3D, vertices may move in all three directions, but their movement is constrained by the contributions to the cost function given in Eq. (15–16), which enforce

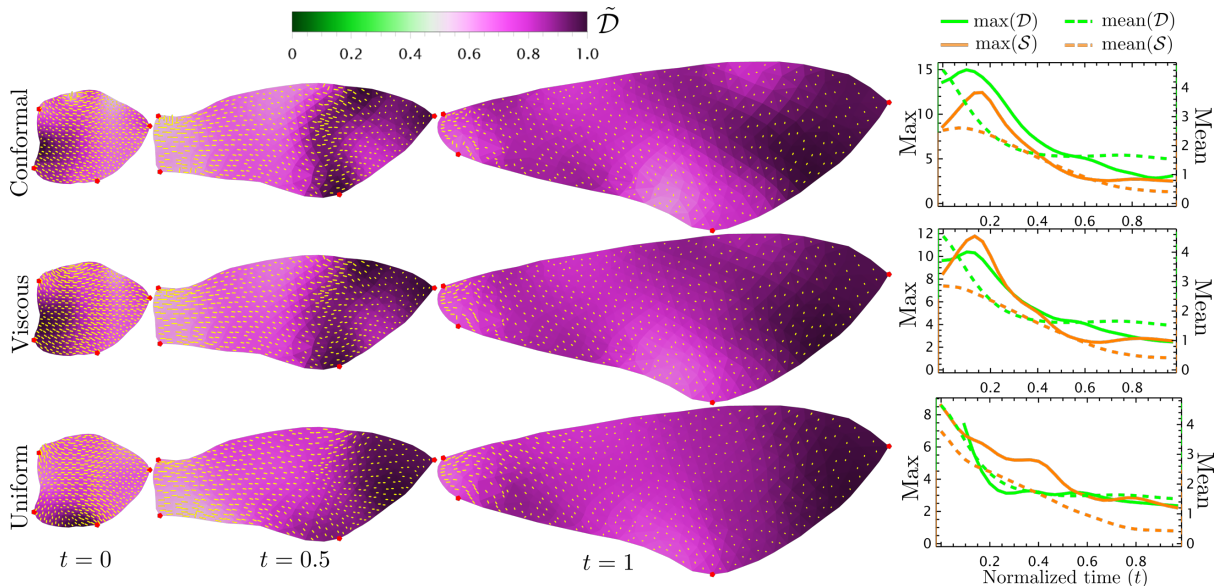


Figure 4: **Optimal 2D quasiconformal flows for *Manduca sexta* (tobacco hawk moth) wings registration with landmarks.** Images of growing *Manduca sexta* wings are taken from [31]. To infer the possible growth patterns, we run the optimization with three different parameter choices given in Table 1: Conformal, Viscous, and Uniform (see the caption of Fig. 3 for details).

the displacement of each vertex to be parallel to the surface and the boundary curve. For closed surfaces (our analysis should work independent of the topology of the surface as long as the flow is smooth), we do not need to enforce boundary displacements and we may run the same three registration models as before (conformal, viscous, uniform). The first example (SI Fig. S3) is a sphere expanding in one direction by a factor of 1.5 and contracting in the other two to preserve volume in the course of 30 time steps. We see that the conformal model (first row in SI Fig. S3) generates nearly conformal flows (small shear rates), where expansion is initially concentrated at the poles of the sphere while contraction dominates in the equator.

The second example we consider (Fig. 6) is a head deforming into a sphere with a linear interpolation in the course of 30 time steps. Unlike the first example (SI Fig. S3), the conformal model when deforming the head does not reduce the shear rate to zero (orange curve in the first row of Fig. 6), which happens at sharp features on the mesh, where it becomes harder to estimate the normal vector and tangent plane to the surface. On the other hand, the uniform model leads to a smoother pattern of dilation and shear rates (both in direction and magnitude), including at sharp features.

#### 4.4 Surfaces with boundary

We test our algorithm on a *persea americana* (avocado) leaf dataset [34], using conformal, viscous, and uniform models (Table 1). We see from the results shown in Fig. 7, that the conformal model leads to low values of the mean shear rate, and therefore a nearly conformal flow. However, it still leads to nonzero shear rate near the tips of the leaf, where the margin deviates from a smooth curve.

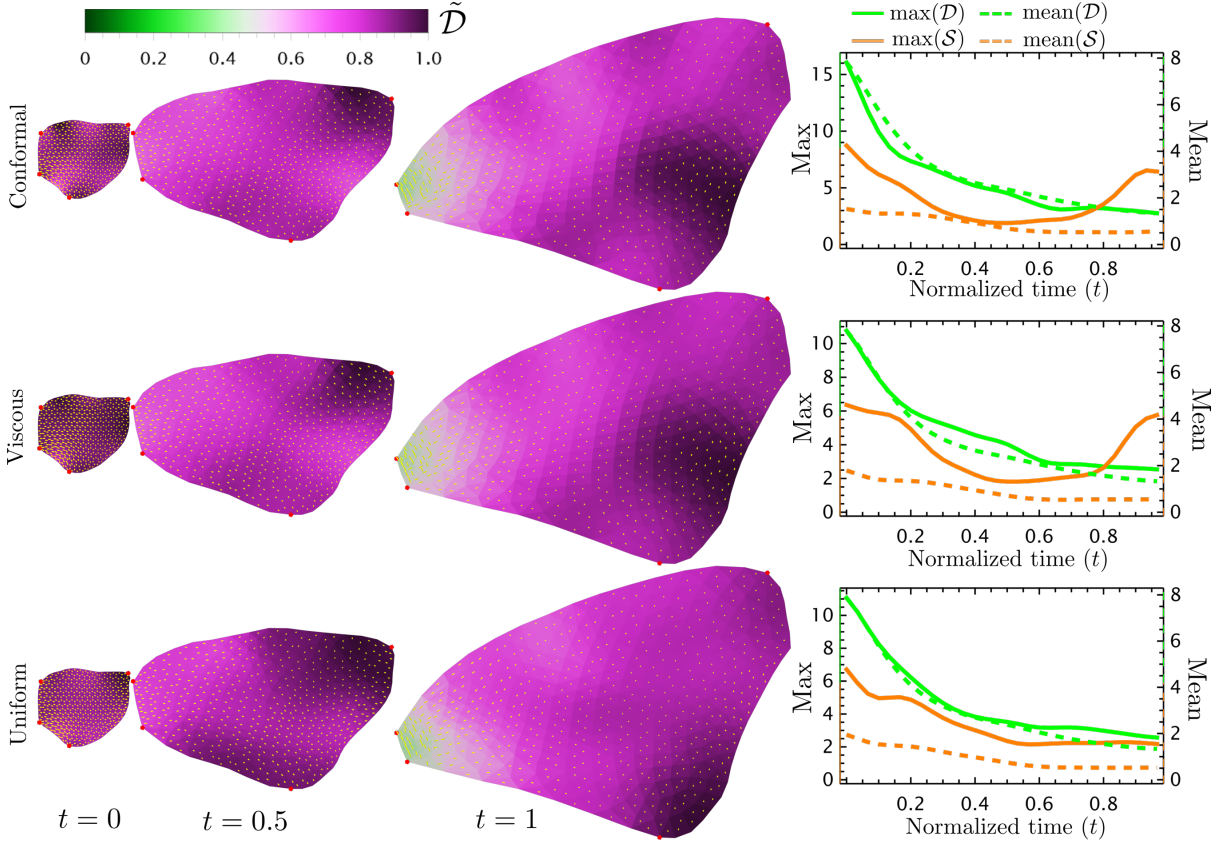


Figure 5: **Optimal 2D quasiconformal flows for *Junonia coenia* (buckeye butterfly) wing registration with landmarks.** Images of growing *Junonia coenia* wings are taken from [31]. To infer the possible growth patterns, we run the optimization with three different parameter choices given in Table 1: Conformal, Viscous, and Uniform (see the caption of Fig. 3 for details).

As before, the inferred growth pattern depends strongly on the model assumed (conformal, viscous, or uniform). Therefore, next we will explore how accounting for the dynamics that generate a given flow can help us better recover growth patterns.

#### 4.5 Fitting to geometric flows

In this section, the parameters in Eq. (12) will be nonzero:  $\lambda_1, \lambda_2, \lambda_3 \neq 0$ . We start by testing the algorithm on a synthetic data set consisting of a cylinder deforming according to the following equation (shown in SI Fig. S5),

$$r(z_3) = (r_0 + r_1 \sin(kz_3)e^{\lambda t}) \hat{r}(\phi) + \left( z_3 - \frac{r_1}{r_0 k} \cos(kz_3) [e^{\lambda t} - 1] \right) L_0 \hat{z}_3, \quad (34)$$

where  $z_3 \in [0, 1]$  is the vertical coordinate increasing along the length of the cylinder,  $\phi \in [0, 2\pi]$  is the azimuthal coordinate,  $\hat{r}$  and  $\hat{z}_3$  are cylindrical basis vectors,  $\lambda = 1$  is a growth rate (multiplied by the duration of the flow  $T$ ),  $r_0 = 0.16$  is the unperturbed cylinder radius,  $r_1 = 0.1r_0$  is the initial amplitude of the deformation, and  $L_0 = 1$  is the initial height of the cylinder. Recall that lengths are normalized by  $L$ , where  $L^2$  is the

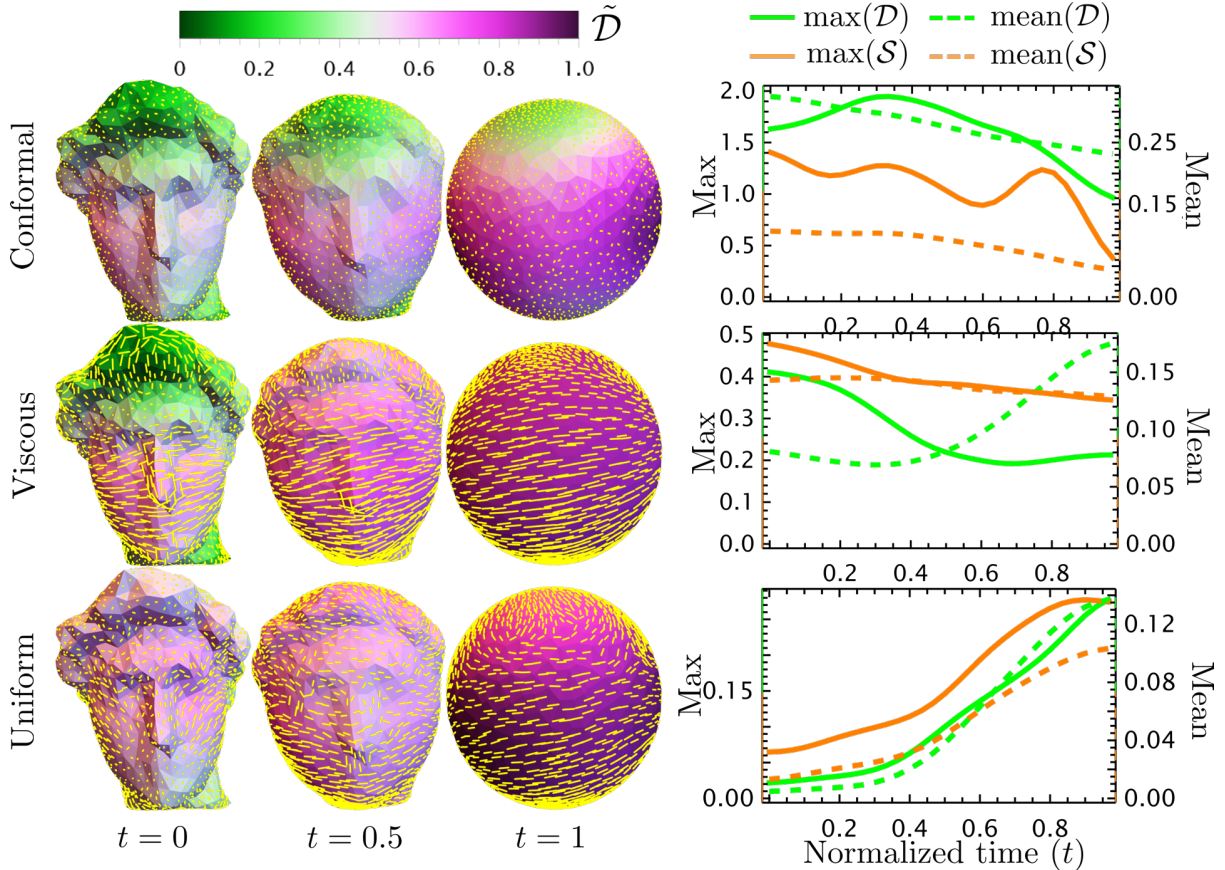


Figure 6: **Optimal 3D quasiconformal flows for closed surfaces.** Here we consider a head mesh evolving towards a sphere. We run the optimization with three different parameter choices given in Table 1: Conformal, Viscous, and Uniform (see the caption of Fig. 3 for details).

area of  $\mathbf{X}(\mathbf{z}, 0)$ . Equation (34) is a solution to  $G_{ij} = 0$ , where  $G_{ij}$  is given in Eq. (12), with  $\lambda_1 = \lambda_2 = 0$ , and  $\lambda_3 = 0.007$ .

To determine whether the dynamical equation  $G_{ij} = 0$  explains the given flow of surfaces  $\mathbf{X}(\mathbf{z}, t)$ , we minimize the cost function in Eq. (20) using the Geometric model parameters given in the last row of Table 1, where  $\lambda_1, \lambda_2, \lambda_3 \neq 0$ , and comparing it to a Viscous model (having the same  $A_1, B_1$  but with  $\lambda_1 = \lambda_2 = \lambda_3 = 0$ ). In addition, we perform separate fits for the Ricci ( $\lambda_1 = \lambda_2 = 0, \lambda_3 \neq 0$ ) and Mean ( $\lambda_1 = \lambda_3 = 0, \lambda_2 \neq 0$ ) curvature flows. To quantify the goodness of fit for each model (Ricci, Mean, Combined, Viscous), we calculate the quantity

$$\eta(t) \equiv \frac{1}{\mathcal{A}(t)} \int d\mathcal{A} g^{ik}(\mathbf{z}, t) g^{jl}(\mathbf{z}, t) G_{ij}(\mathbf{z}, t) G_{jk}(\mathbf{z}, t), \quad (35)$$

where  $\mathcal{A}(t) \equiv \int d\mathcal{A}$  is the total area at time  $t$ . As a consistency check, we find that the Geometric and Ricci models, when applied to the growing cylinder data set, significantly reduce the growth cost (SI Fig. S4–S5), especially for early times, as expected since the data set was generated using Eq. (34), which is an approximate solution to the Ricci flow. Furthermore, the Ricci fit recovers the value  $\lambda_3 \approx 0.007$  (with less 3% error).

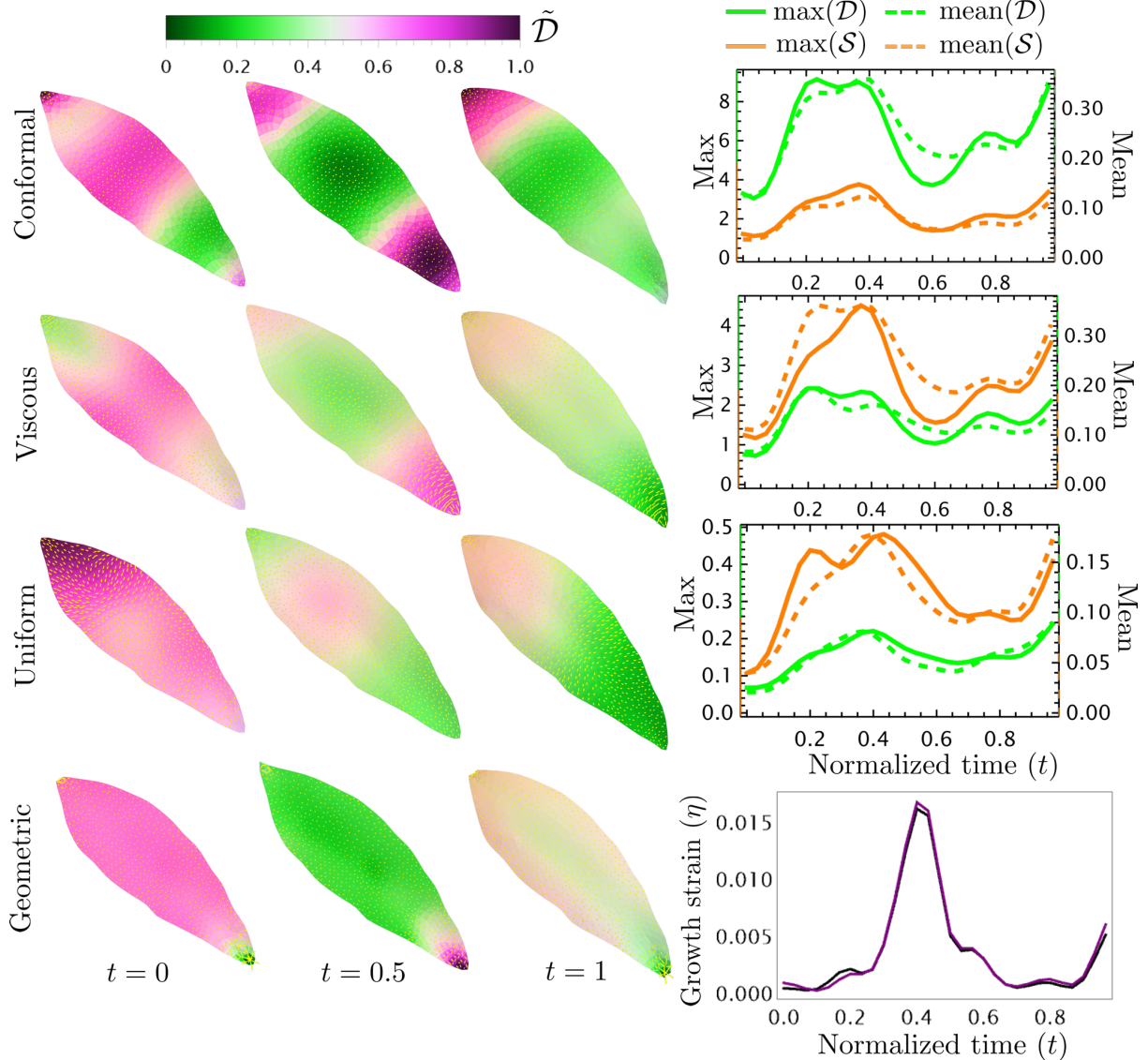


Figure 7: **Optimal 3D quasiconformal flows using geometric flows for growing leaves.** Leaf data was taken from [34] and processed as described in the main text and Fig. 2. We run the optimization with four different parameter choices given in Table 1: Conformal, Viscous, Uniform, and Geometric. Here  $\mathcal{D}$  is the dilation rate given in Eq. (9) and  $\mathcal{S}$  is the shear rate given in Eq. (10). The triangles are color-coded according to the normalized dilation rate,  $\tilde{\mathcal{D}} \equiv \mathcal{D} / \max(\mathcal{D}, \mathcal{S})$ , while the length of the yellow line segments represents the magnitude of normalized shear rate,  $\tilde{\mathcal{S}} \equiv \mathcal{S} / \max(\mathcal{D}, \mathcal{S})$ , and their direction is along the largest eigen direction of the strain rate tensor. The last column shows the maximum and mean dilation and shear rates plotted against normalized time for the different registrations in each row. The plot on the lower right gives the magnitude of the growth cost, which is defined as  $\eta(t) \equiv \langle \text{Tr}[G_{ij}^2(\mathbf{z}, t)] \rangle$ , where the angle brackets represent averaging over the area of the surface, as given in Eq. (35).

The last row of Fig. 7 shows the results for a growing leaf. While we obtain a correlation between curvature and dilation rate, the minimum growth cost  $\mathcal{C}_{growth}$  is not significantly

reduced in the Geometric model. This implies that while growth rate is correlated with curvature in leaves, the equation  $G_{ij} = 0$  is not sufficient to explain the entire growth pattern, some of which may be prescribed in-plane growth that is not curvature dependent or is triggered by movement of the mid-vein as described, for example, in [34].

## 5 Conclusions

Understanding the continuous growth process of biological shapes is a central problem in biology. In this paper, we extended the notion of  $K$ -quasiconformal map to  $k$ -quasiconformal flows and provided a general algorithm for inferring growth patterns using a diverse set of criteria, including local geometric distortions, spatial variations, and fits to dynamical equations, such as geometric flows. Experimental results on different 2D and 3D shapes have demonstrated the effectiveness of our framework, suggesting that our framework is useful whenever a growing structure — in nature or industry — is observed but the identities of individual points are not tracked over time (except possibly for a small set of landmarks).

Future work will explore the problem of determining an optimal quasiconformal flow for more sparse temporal data. In addition, future work will extend the set of dynamical laws that can be tested using our framework, for example those that involve nonlocal feedback between mechanical stress and growth [26, 40].

## References

- [1] D. W. Thompson, *On growth and form*, vol. 1. Cambridge university press Cambridge, 1917.
- [2] L. V. Ahlfors, “Complex analysis: an introduction to the theory of analytic functions of one complex variable,” *New York, London*, vol. 177, 1953.
- [3] E. Sharon and D. Mumford, “2D-shape analysis using conformal mapping,” *Int. J. Comput. Vis.*, vol. 70, no. 1, pp. 55–75, 2006.
- [4] B. Lévy, S. Petitjean, N. Ray, and J. Maillot, “Least squares conformal maps for automatic texture atlas generation,” *ACM Trans. Graph.*, vol. 21, no. 3, pp. 362–371, 2002.
- [5] M. Desbrun, M. Meyer, and P. Alliez, “Intrinsic parameterizations of surface meshes,” *Comput. Graph. Forum*, vol. 21, no. 3, pp. 209–218, 2002.
- [6] G. Mitchison, “Conformal growth of Arabidopsis leaves,” *J. Theor. Biol.*, vol. 408, pp. 155–166, 2016.
- [7] V. Alba, J. E. Carthew, R. W. Carthew, and M. Mani, “Global constraints within the developmental program of the drosophila wing,” *Elife*, vol. 10, p. e66750, 2021.
- [8] X. Gu, Y. Wang, T. F. Chan, P. M. Thompson, and S.-T. Yau, “Genus zero surface conformal mapping and its application to brain surface mapping,” *IEEE Trans. Med. Imaging*, vol. 23, no. 8, pp. 949–958, 2004.

- [9] P. T. Choi, K. C. Lam, and L. M. Lui, “FLASH: Fast landmark aligned spherical harmonic parameterization for genus-0 closed brain surfaces,” *SIAM J. Imaging Sci.*, vol. 8, no. 1, pp. 67–94, 2015.
- [10] D. Kierzkowski, A. Runions, F. Vuolo, S. Strauss, R. Lymbouridou, A.-L. Routier-Kierzkowska, D. Wilson-Sanchez, H. Jenke, C. Galinha, G. Mosca, *et al.*, “A growth-based framework for leaf shape development and diversity,” *Cell*, vol. 177, no. 6, pp. 1405–1418, 2019.
- [11] F. Zhao, F. Du, H. Oliveri, L. Zhou, O. Ali, W. Chen, S. Feng, Q. Wang, S. Lü, M. Long, *et al.*, “Microtubule-mediated wall anisotropy contributes to leaf blade flattening,” *Curr. Biol.*, vol. 30, no. 20, pp. 3972–3985, 2020.
- [12] L. V. Ahlfors, *Lectures on quasiconformal mappings*, vol. 38. American Mathematical Soc., 2006.
- [13] G. W. Jones and L. Mahadevan, “Planar morphometry, shear and optimal quasiconformal mappings,” *Proc. R. Soc. A*, vol. 469, no. 2153, p. 20120653, 2013.
- [14] G. P. T. Choi and L. Mahadevan, “Planar morphometrics using Teichmüller maps,” *Proc. R. Soc. A*, vol. 474, no. 2217, p. 20170905, 2018.
- [15] G. P. T. Choi, H. L. Chan, R. Yong, S. Ranjitkar, A. Brook, G. Townsend, K. Chen, and L. M. Lui, “Tooth morphometry using quasi-conformal theory,” *Pattern Recognit.*, vol. 99, p. 107064, 2020.
- [16] G. P. T. Choi, D. Qiu, and L. M. Lui, “Shape analysis via inconsistent surface registration,” *Proc. R. Soc. A*, vol. 476, no. 2242, p. 20200147, 2020.
- [17] E. Klassen, A. Srivastava, M. Mio, and S. H. Joshi, “Analysis of planar shapes using geodesic paths on shape spaces,” *IEEE Trans. Pattern Anal. Mach. Intell.*, vol. 26, no. 3, pp. 372–383, 2004.
- [18] M. F. Beg, M. I. Miller, A. Trouvé, and L. Younes, “Computing large deformation metric mappings via geodesic flows of diffeomorphisms,” *Int. J. Comput. Vis.*, vol. 61, pp. 139–157, 2005.
- [19] A. Srivastava and E. P. Klassen, *Functional and shape data analysis*, vol. 1. Springer, New York, 2016.
- [20] A. B. Tumpach, H. Drira, M. Daoudi, and A. Srivastava, “Gauge invariant framework for shape analysis of surfaces,” *IEEE Trans. Pattern Anal. Mach. Intell.*, vol. 38, no. 1, pp. 46–59, 2015.
- [21] I. H. Jermyn, S. Kurtek, E. Klassen, and A. Srivastava, “Elastic shape matching of parameterized surfaces using square root normal fields,” in *Computer Vision—ECCV 2012: 12th European Conference on Computer Vision, Florence, Italy, October 7–13, 2012, Proceedings, Part V 12*, pp. 804–817, Springer, 2012.
- [22] R. S. Hamilton, “The Ricci flow on surfaces, mathematics and general relativity,” *Contemp. Math.*, vol. 71, pp. 237–261, 1988.

- [23] W. W. Mullins, “Two-dimensional motion of idealized grain boundaries,” *J. Appl. Phys.*, vol. 27, no. 8, pp. 900–904, 1956.
- [24] F. Chang and K. C. Huang, “How and why cells grow as rods,” *BMC Biol.*, vol. 12, no. 1, p. 54, 2014.
- [25] S. Al-Mosleh, A. Gopinathan, C. D. Santangelo, K. C. Huang, and E. R. Rojas, “Feedback linking cell envelope stiffness, curvature, and synthesis enables robust rod-shaped bacterial growth,” *Proc. Natl. Acad. Sci.*, vol. 119, no. 41, p. e2200728119, 2022.
- [26] S. al Mosleh and L. Mahadevan, “How to grow a flat leaf,” *Phys. Rev. Lett.*, vol. 131, no. 9, p. 098401, 2023.
- [27] S. Al-Mosleh, G. P. T. Choi, A. Abzhanov, and L. Mahadevan, “Geometry and dynamics link form, function, and evolution of finch beaks,” *Proc. Natl. Acad. Sci.*, vol. 118, no. 46, p. e2105957118, 2021.
- [28] S. Al Mosleh, A. Gopinathan, and C. Santangelo, “Growth of form in thin elastic structures,” *Soft Matter*, vol. 14, no. 41, pp. 8361–8371, 2018.
- [29] M. Webster and H. D. Sheets, “A practical introduction to landmark-based geometric morphometrics,” *The Paleontological Society Papers*, vol. 16, pp. 163–188, 2010.
- [30] M. P. Do Carmo, *Differential geometry of curves and surfaces: revised and updated second edition*. Courier Dover Publications, 2016.
- [31] H. F. Nijhout, M. Cinderella, and L. W. Grunert, “The development of wing shape in Lepidoptera: mitotic density, not orientation, is the primary determinant of shape,” *Evol. Dev.*, vol. 16, no. 2, pp. 68–77, 2014.
- [32] P.-O. Persson and G. Strang, “A simple mesh generator in MATLAB,” *SIAM Rev.*, vol. 46, no. 2, pp. 329–345, 2004.
- [33] D.-J. Kroon, “2D Line Curvature and Normals.” <https://www.mathworks.com/matlabcentral/fileexchange/32696-2d-line-curvature-and-normals>, 2011.
- [34] J. Derr, R. Bastien, É. Couturier, and S. Douady, “Fluttering of growing leaves as a way to reach flatness: experimental evidence on *Persea americana*,” *J. R. Soc. Interface*, vol. 15, no. 138, p. 20170595, 2018.
- [35] G. Taubin, “Curve and surface smoothing without shrinkage,” in *Proceedings of IEEE International Conference on Computer Vision*, pp. 852–857, IEEE, 1995.
- [36] C. Loop, “Smooth subdivision surfaces based on triangles,” *Master’s thesis, University of Utah, Department of Mathematics*, 1987.
- [37] D.-J. Kroon, “Curvature estimation on triangle mesh.” <https://www.mathworks.com/matlabcentral/fileexchange/32573-patch-curvature>, 2018.

- [38] B. Friedrich, “frenet\_robust.” [https://www.mathworks.com/matlabcentral/fileexchange/47885-frenet\\_robust-zip](https://www.mathworks.com/matlabcentral/fileexchange/47885-frenet_robust-zip), 2014.
- [39] P. N. Swarztrauber, D. L. Williamson, and J. B. Drake, “The Cartesian method for solving partial differential equations in spherical geometry,” *Dyn. Atmos. Oceans*, vol. 27, no. 1-4, pp. 679–706, 1998.
- [40] K. Harline, A. Fruleux, B. Lane, G. Mosca, S. Strauss, N. Tavakolian, J. W. Satterlee, C.-B. Li, A. Singh, R. S. Smith, *et al.*, “Dynamic growth re-orientation orchestrates flatness in the Arabidopsis leaf,” *BioRxiv*, pp. 2022–11, 2022.